

Vortex penetration into micron-sized $\text{Bi}_2\text{Sr}_2\text{CaCu}_2\text{O}_{8+\delta}$

Y. M. Wang and A. Zettl

*Department of Physics, University of California at Berkeley, Berkeley, California 94720
and Materials Sciences Division, Lawrence Berkeley National Laboratory, Berkeley, California 94720*

S. Ooi and T. Tamegai

*Department of Applied Physics, The University of Tokyo, Hongo, Bunkyo-ku, Tokyo 113-8656, Japan
(Received 16 November 2001; published 18 April 2002)*

The onset of vortex penetration into micron-sized $\text{Bi}_2\text{Sr}_2\text{CaCu}_2\text{O}_{8+\delta}$ disks and squares is studied using local magnetization measurements. The vortex penetration field H_p is observed to exceed the lower critical field H_{c1} at all temperatures below the superconducting transition temperature T_c . The magnitude of H_p is determined by sample size and geometry. Below 15 K, H_p is approximately proportional to the sample width D , consistent with the Bean bulk pinning model. Above 15 K, H_p is a function of the sample thickness-to-width ratio t/D , and agrees with the Bean-Livingston surface-barrier effect.

DOI: 10.1103/PhysRevB.65.184506

PACS number(s): 74.60.Ec, 74.60.Ge

In type-II superconductors, the lower critical field H_{c1} separates the Meissner state from the vortex state. At H_{c1} , the formation of vortices becomes energetically favorable. However, when a vortex tries to enter the sample, it encounters additional energy barriers created by the sample's boundary. A magnetic field different from H_{c1} is required for a vortex to overcome these barriers. When the required magnetic field is higher than H_{c1} , a vortex penetration field H_p higher than H_{c1} is observed in experiments. Investigation of H_p should provide direct information concerning the energy barriers acting against the entering vortices, which in turn should lead to a better understanding of the vortex entry mechanism in type-II superconductors.

The energy barriers against the entering vortices consist of a geometrical barrier,¹⁻³ a Bean-Livingston surface barrier,⁴⁻⁶ and a bulk-pinning energy barrier.^{7,8} The geometrical barrier and the Bean-Livingston surface barrier together are called surface barriers. Various models show that both the surface barriers and the bulk-pinning barrier vary with sample size and geometry, though differently because of their different origins. The geometrical barrier is caused by the competition between two forces on a vortex: the inward Lorentz force due to the Meissner shielding current and the outward force due to line tension.¹⁻³ It varies with the sample thickness-to-width ratio t/D .^{3,9-12} The Bean-Livingston surface barrier, which is the result of the outward attractive force on a vortex by its image, also depends on t/D , though indirectly through the demagnetization factor.⁴⁻⁶ The bulk-pinning energy barrier is caused by point impurity pinning in the sample. It increases with the sample width D .^{7,8} By studying the variation of H_p with sample size and shape, one can experimentally obtain the sample geometry dependence of the above energy barriers.

In this paper, we investigate the vortex penetration field H_p in the high T_c superconductor $\text{Bi}_2\text{Sr}_2\text{CaCu}_2\text{O}_{8+\delta}$ (BSCCO). The high anisotropy associated with BSCCO makes a study of H_p particularly desirable. However, experimental studies of H_p in BSCCO have been challenging due to the difficulty associated with fabricating small samples. In particular, the typical thickness of BSCCO single crystals is

of order 10 μm and the surface barriers are functions of t/D . Thus, in order for t/D to be of order unity, the width of a sample must be micron sized.

Using photolithography and Ar^+ -ion milling, we have developed a technique suitable for machining BSCCO single crystals into micron-sized samples. H_p has been measured for such samples using local magnetization measurements. It is observed that H_p varies with sample size and geometry at all temperatures below T_c . We compare H_p to theoretical model predictions in an attempt to identify, for a given temperature, the dominant barrier against vortex penetration. Below 15 K, $H_p \propto D$, in agreement with the Bean bulk-pinning model. At temperatures above 15 K, $H_p \propto \sqrt{t/D}$, H_p is consistent with the Bean-Livingston surface-barrier model.

Experimental magnetization data were obtained using a local Hall-effect probe as described previously.¹³ The Hall sensor has an active area of $10 \times 10 \mu\text{m}^2$. Single crystals of BSCCO were grown using the floating-zone method.¹⁴ The crystals were cleaved into 10- μm -thick pieces from which disks and squares of lateral dimensions ranging from 20 μm to 180 μm were then microfabricated. Since the sample microfabrication method is nonstandard, we describe it in detail here.

The challenge of machining micron-sized BSCCO lies in the deep etching of small patterns. Previous methods using Ar^+ -ion milling and photolithography etch up to 10 nm in BSCCO at which point the photoresist begins to burn.¹⁵ Deeper etching is harder to achieve with burned photoresist; in addition, the removal of the burned photoresist after etching is difficult. By introducing an annealing procedure before the ion milling step, and using a thicker photoresist (Shipley 5740), we routinely successfully etch samples up to 10 μm thick.

Figure 1 shows the schematic of the fabrication process. The photoresist preannealing step (30 min at 100 °C) is applied after patterning the sample [Fig. 1(a)] and before starting the ion milling process [Fig. 1(b)]. The preannealing prevents photoresist from burning during the milling process. The etch rate of preannealed photoresist is lower than that of

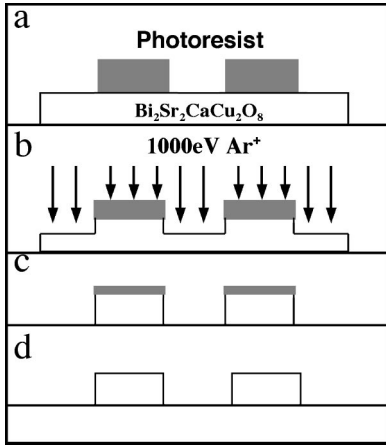


FIG. 1. Schematics of fabricating micron-sized BSCCO. (a) Patterning photoresist on the sample surface. (b) BSCCO, together with the photoresist, is exposed to 1000-eV Ar^+ ion bombardment. (c) The Ar^+ bombardment stops when the sample is etched all the way through. (d) The remaining photoresist is dissolved away using acetone.

BSCCO, enabling one to mill for hours until the $10\ \mu\text{m}$ -thick single crystal is completely etched through. After the ion milling, the preannealed photoresist is washed away using acetone [Fig. 1(c)] and the original smooth surface of BSCCO is restored [Fig. 1(d)]. Figures 2(a) and 2(b) show an ion milled BSCCO square and disk, respectively. We note that by varying the size and shape of the photoresist, different structures may be created in a range of materials, such as a pyramid array in BSCCO and a cone in silicon, shown in Figs. 2(c) and 2(d), respectively.

For the present study, ion milled samples of BSCCO were slightly overdoped ($T_c = 87\ \text{K}$) after fabrication by annealing in air at 550°C for 20 h. The local magnetization of the samples was determined by placing the samples in a superconducting solenoid with the applied field H_a parallel to the crystal c axis. All local magnetization measurements were taken at the face center of the sample using the microfabricated GaAs/AlGaAs Hall sensor.¹⁶ Local magnetization measurements on zero-field-cooled samples were made at a

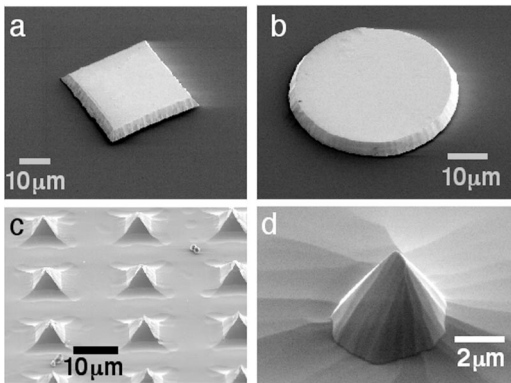


FIG. 2. Scanning electron microscope image of a micromachined (a) square, (b) disk, (c) pyramid array in BSCCO, and (d) a cone in silicon.

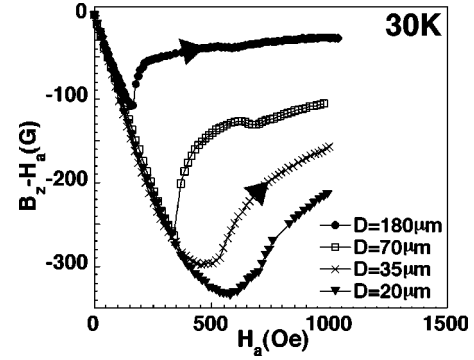


FIG. 3. B_z-H_a vs H_a of BSCCO disks with diameter D of $20\ \mu\text{m}$, $35\ \mu\text{m}$, $70\ \mu\text{m}$, and $180\ \mu\text{m}$ at $30\ \text{K}$. H_p is defined as the H_a at the first peak of the B_z-H_a vs H_a curve. We attribute the early deviation from linearity of the $20\text{-}\mu\text{m}$ and $35\text{-}\mu\text{m}$ disks to the comparable size of the sample and the Hall sensor area. The arrow-head indicates the field-sweep direction.

magnetic-field ramp rate of $1(\text{Oe/s})$ for both increasing and decreasing field.

Figure 3 shows the local magnetization, B_z-H_a vs applied field H_a at $30\ \text{K}$ for $10\text{-}\mu\text{m}$ -thick BSCCO disks with diameter D ranging from $20\ \mu\text{m}$ to $180\ \mu\text{m}$, where B_z is the local magnetic induction. H_a at the first peak of the B_z-H_a vs H_a curve is defined as the vortex penetration field H_p . Since the Hall sensor is located under the center of the sample, the H_p reported here measures the full vortex penetration field, representing the magnetic field at which the vortices reach the center of the sample. As shown in Fig. 3, at $30\ \text{K}$ H_p increases as the diameter of the sample becomes smaller. The measurements of Fig. 3 have been repeated for square- and disk-shaped samples at temperatures ranging from $5\ \text{K}$ to $83\ \text{K}$. H_p exhibits distinctively different sample size dependences above and below $15\ \text{K}$.

Above $15\ \text{K}$, H_p decreases with sample size as a function of $\sqrt{t/D}$. Figure 4 displays H_p vs $\sqrt{t/D}$ for BSCCO (a) disks and (b) squares at selected temperatures above $15\ \text{K}$. The solid lines are linear fits of H_p to $\sqrt{t/D}$ in units of Oe

$$H_p = H'_{c1}(-0.2 + 7\sqrt{t/D}), \quad (1)$$

for BSCCO disks and

$$H_p = H'_{c1}(-0.6 + 7\sqrt{t/D}), \quad (2)$$

for BSCCO squares, respectively, where H'_{c1} is the adjusted lower critical field taking into account the surface-barrier effects at a field ramp rate of $1(\text{Oe/s})$.¹⁷ $H'_{c1} \approx 170\ \text{Oe}$, $120\ \text{Oe}$, and $5\ \text{Oe}$ at $20\ \text{K}$, $30\ \text{K}$, and $83\ \text{K}$, respectively.¹⁷

Figure 5 shows the B_z-H_a vs H_a curves of a $50\ \mu\text{m}$ BSCCO square at selected temperatures ranging from $15\ \text{K}$ to $78\ \text{K}$. As temperatures increases, H_p decreases. H_p vs T is plotted in Fig. 6. H_p vs T of a $90\ \mu\text{m}$ square is also plotted for the purpose of comparison with the $50\ \mu\text{m}$ square. The solid lines below $15\ \text{K}$ in Fig. 6 are exponential fits of H_p as a function of temperature. The exponential fits of the $50\ \mu\text{m}$ and the $90\ \mu\text{m}$ squares meets at $15\ \text{K}$, therefore we consider $15\ \text{K}$ to be the transition point at which the behavior of H_p

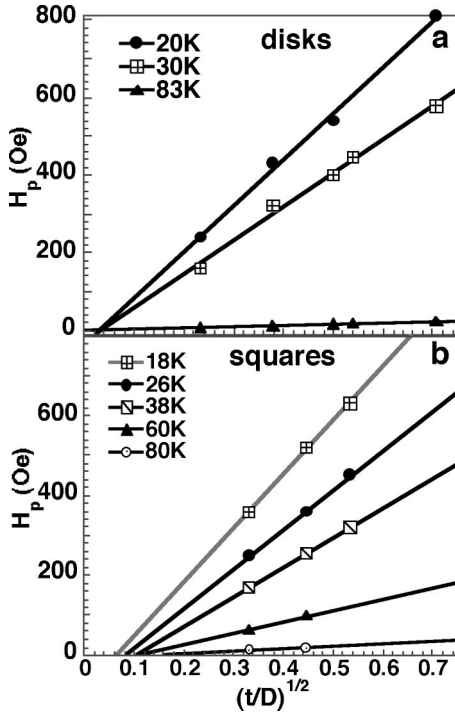


FIG. 4. Vortex penetration field H_p vs $\sqrt{t/D}$ for BSCCO (a) disks and (b) squares at selected temperatures, where D represents the diameter of a BSCCO disk and the width of a square, respectively. The lines are the linear fits of H_p to $\sqrt{t/D}$ (see text).

changes: $H_p(90 \mu\text{m}) \geq H_p(50 \mu\text{m})$ below 15 K and vice versa above 15 K; H_p increases abruptly below 15 K and is smooth above 15 K. In the following sections, we discuss separately H_p at temperatures above and below 15 K.

Above 15 K, the bulk-pinning energy barrier is negligible,¹¹ so we consider only the surface barriers when analyzing H_p . Since the surface barriers are assumed to be functions of $\sqrt{t/D}$,^{3,5,6,9-12} we plot, for the purpose of comparison with the surface-barrier models, H_p vs $\sqrt{t/D}$ as shown in Fig. 4. Brandt's geometrical barrier calculation of pin-free BSCCO disks¹⁰ predicts

$$H_{p(GB)} = H_{c1} \tanh[0.67 \sqrt{t/D}]. \quad (3)$$

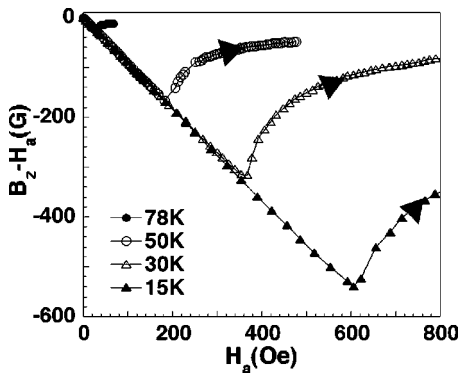


FIG. 5. $B_z - H_a$ vs H_a for the 50- μm BSCCO square at various temperatures. H_p is inversely proportional to temperature.

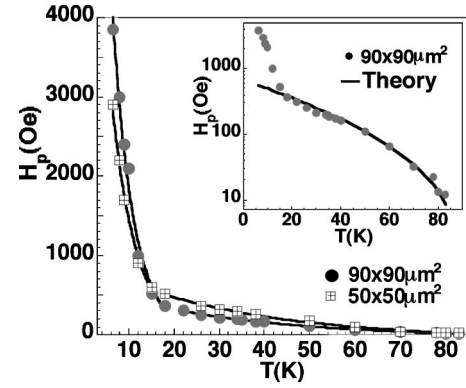


FIG. 6. H_p vs T for the 50- μm and 90- μm BSCCO squares. Below 15 K, $H_p(90 \mu\text{m}) \geq H_p(50 \mu\text{m})$, and vice versa above 15 K. The solid lines below 15 K are the exponential fits of H_p to temperature (see text). The inset compares $H_{p(SB)}$ with H_p of the 90- μm square in a logarithmic scale.

Using the 20- μm disk at 30 K as an example, we obtain from Eq. (3) $H_{p(GB)} = 63$ Oe with $H_{c1} = H'_{c1} = 120$ Oe.¹⁷ It is eightfold smaller than our experimental value of $H_p = 522$ Oe. Comparison at other temperatures above 15 K yields similar results. On the other hand, Kuznetsov's geometrical barrier calculation for type-II superconductor disks with pinning predicts

$$H_{p(GB)} = H_{c1} \frac{\sqrt{\eta/\alpha}}{N}, \quad (4)$$

where η is a dimensionless parameter, α is the width-to-thickness ratio D/t of the disk, and N is the enhancement factor.⁹ Given that $\sqrt{\eta}/N$ is of order unity for our sample sizes,⁹ $H_{p(GB)}$ is sixfold lower than our experimental H_p . Thus, the geometrical barrier is ruled out as the dominating energy barrier at temperatures above 15 K for micron-sized BSCCO.

We now consider whether the Bean-Livingston surface-barrier vortex penetration field H_p determines H_p at temperatures above 15 K. The Bean-Livingston model predicts

$$H_{p(SB)} = \sqrt{t/D} H_c(T) \exp(-T/T_0), \quad (5)$$

where H_c is the thermodynamic critical field and T_0 is the characteristic temperature.⁵ The magnitudes of the Bean-Livingston $H_{p(SB)}$ and our experimental H_p are comparable. We compare the temperature dependences in the inset to Fig. 6 for a 90- μm disk. By using $H_c \approx \kappa / \ln \kappa H_{c1}$,⁶ where $\kappa = \lambda/\xi$ is the ratio of the penetration depth λ and the coherent length ξ , and $H_{c1}(T) = H_{c1}(0) [1 - (T/T_c)^2]$,¹⁸ Eq. (5) can be written as $H_{p(SB)} = \sqrt{t/D} \kappa / \ln \kappa H_{c1}(0) [1 - (T/T_c)^2] \exp(-T/T_0)$. The solid line in the inset to Fig. 6 is the best fit of $H_{p(SB)}$ to the 90- μm square, which gives reasonable fitting parameters: $T_0 = 35$ K⁵ and $\kappa / \ln \kappa H_{c1}(0) \approx 2000$ Oe, knowing that $\kappa / \ln \kappa \rightarrow \sim 10^6$ and $H_{c1}(0) \approx 200$ Oe.¹¹ $H_{p(SB)}$ agree well with H_p above 15 K. Similar agreements are obtained for other sized samples. We conclude that above 15 K, H_p in micron-sized BSCCO is determined by the Bean-Livingston surface-barrier effect.

Below 15 K, H_p rises sharply and is approximately proportional to the sample width D as shown in the main body of Fig. 6. The Bean bulk-pinning model prediction of H_p is^{8,18}

$$H_{p(BP)} = 2\pi J_c D / c, \quad (6)$$

where the critical current $J_c(T) \approx J_c(0) \exp(-T/T_1)$,⁹ T_1 is the critical current temperature exponent and ~ 10 K, and c is the speed of light. The solid lines below 15 K in Fig. 6 are exponential fits of H_p as a function of temperature,

$$H_p \approx 186D(\mu\text{m}) \exp(-T/5 \text{ K})(Oe). \quad (7)$$

When comparing with Eq. (6), Eq. (7) gives reasonable values¹⁸ of $J_c(0) \approx 3 \times 10^6$ (A/cm²) and $T_1 = 5$ K.¹⁹ We consider H_p to be in reasonably good agreement with $H_{p(BP)}$ below 15 K.

We thus find that for BSCCO of our sample sizes, below 15 K, the Bean bulk-pinning energy barrier determines the vortex penetration field; above 15 K, the Bean-Livingston surface-barrier effect dominates.²⁰ In larger samples, the sample thickness to width ratio t/D decreases. Thus, at a given temperature, the dominating energy barrier can differ from that in BSCCO of our sample sizes.

We thank Misha Indenbom and Alex Koshelev for helpful discussion. This research was supported in part by NSF Grants Nos. DMR-9801738 and DMR-9501156, by the Director of the Office of Energy Research, Office of Basic Energy Sciences, Materials Sciences Division of the US Department of Energy under Contract No. DEAC03-76SF00098, and by CREST and Grant-in-Aid for Scientific Research from the Ministry of Education, Science, Sports and Culture of Japan.

¹M.V. Indenbom, G. D'Anna, M.O. Andre, V.V. Kabanov, and W. Benoit, *Physica C* **235-240**, 201 (1994).
²E. Zeldov, A.I. Larkin, V.B. Geshkenbein, M. Konczykowski, D. Majer, B. Khaykovich, V.M. Vinokur, and H. Shtrikman, *Phys. Rev. Lett.* **73**, 1428 (1994).
³M. Benkraouda and J.R. Clem, *Phys. Rev. B* **53**, 5716 (1996).
⁴C.P. Bean and J.D. Livingston, *Phys. Rev. Lett.* **12**, 14 (1964).
⁵L. Burlachkov, V.B. Geshkenbein, A.E. Koshelev, A.I. Larkin, and V.M. Vinokur, *Phys. Rev. B* **50**, 16770 (1994).
⁶L. Burlachkov, *Phys. Rev. B* **47**, 8056 (1993).
⁷G. Blatter, M.V. Feigel'man, V.B. Geshkenbein, A.I. Larkin, and V.M. Vinokur, *Rev. Mod. Phys.* **66**, 1125 (1994).
⁸C.P. Bean, *Phys. Rev. Lett.* **8**, 250 (1962).
⁹A.V. Kuznetsov, D.V. Eremenko, and V.N. Trofimov, *Phys. Rev. B* **56**, 9064 (1997).
¹⁰E.H. Brandt, *Phys. Rev. B* **60**, 11 939 (1999).
¹¹E. Zeldov, D. Majer, M. Konczykowski, A.I. Larkin, V.M. Vinokur, V.B. Geshkenbein, N. Chikumoto, and H. Shtrikman, *Europhys. Lett.* **30**, 367 (1995).

Phys. Lett. **30**, 367 (1995).
¹²E.H. Brandt, *Phys. Rev. B* **59**, 3369 (1999).
¹³Y.M. Wang, M.S. Fuhrer, A. Zettl, S. Ooi, and T. Tamegai, *Phys. Rev. Lett.* **86**, 3626 (2001).
¹⁴S. Ooi, T. Shibauchi, and T. Tamegai, *Physica C* **302**, 339 (1998).
¹⁵A. Yurgens, M. Konczykowski, N. Mros, D. Winkler, and T. Claesson, *Phys. Rev. B* **60**, 12 480 (1999).
¹⁶E. Zeldov, D. Majer, M. Konczykowski, V.B. Geshkenbein, V.M. Vinokur, and H. Shtyrikman, *Nature (London)* **375**, 373 (1995).
¹⁷M. Nideröst, R. Frassanito, M. Saalfrank, A.C. Mota, G. Blatter, V.N. Zavaritsky, T.W. Li, and P.H. Kes, *Phys. Rev. Lett.* **81**, 3231 (1998).
¹⁸M. Tinkham, *Introduction to Superconductivity*, 2nd ed. (McGraw-Hill, New York, 1996).
¹⁹ $T_1 = 5$ K is consistent with our previous result of T_1 in Ref. 13.
²⁰The distributed surface-barrier model [N. Morozov, E. Zeldov, M. Konczykowski, and R.A. Doyle, *Physica C* **291**, 113 (1997)] also supports our results.